Regular Article - Flowing Matter

Aerodynamic wall shear fluctuation in sand-laden flow in a turbulent boundary layer

Wei He[1,2,a], Ning Huang[1,2], and Jie Zhang[1,2,b]

[1] Key Laboratory of Mechanics on Disaster and Environment in Western China, Ministry of Education of China, Lanzhou University, Lanzhou 730000, China
[2] College of Civil Engineering and Mechanics, Lanzhou University, Lanzhou 730000, China

Abstract
To improve our understanding on the aerodynamic wall shear fluctuation in particle-laden flow, we perform statistical and spectral analyses of aerodynamic wall shear fluctuation in sand-free and sand-laden flows in a turbulent boundary layer based on the results of a wind tunnel experiment. An increase in the skewness of the probability density function of aerodynamic wall shear fluctuation is found in the sand-laden flow. The turbulent intensity of aerodynamic wall shear stress increases rapidly with the sand mass flux. The decreased convective velocity indicates blocking effects of sand particles in the near-wall region. The power of aerodynamic wall shear fluctuation in the sand-laden flow increases at low frequencies corresponding to the duration of sand streamers. The results of a superstatistical analysis of skin friction velocity show that spatio-temporal fluctuation in the local energy dissipation rate is enhanced in the sand-laden flow. Finally, the local and spatio-drifting force acting on the stochastic system of wall shear fluctuation in sand-laden flow are different, providing a proof for the significant variation in flow condition caused by sand streamers near the wall

1 Introduction

Aerodynamic wall shear stress (τ_{a}) is an essential parameter of wall-bounded flow. In environmental flows, such as air-sand flows, τ_{a} is of significant ecological and geomorphological importance, as it is connected to erosion, bed transformation, sediment transportation, the transport of interfacial gas and nutrients, and so on [1,2].

Time-averaged aerodynamic wall shear stress $(\bar{\tau}_{\mathrm{a}})$ has been thoroughly studied both theoretically and experimentally. The parameter τ_{a} is often expressed as a function of skin friction velocity, $u_{\tau} = \sqrt{\tau_{\mathrm{a}}/\rho}$, and the skin friction velocity has been used as the scaling velocity in the boundary layer dating back to Prandtl (1905) [3]. Various relationships between $\bar{\tau}_{\mathrm{a}}$ and the Reynolds number have been proposed [4,5]. However, aerodynamic wall shear stress always fluctuates in wall-bounded flow [6], and the relationship between the considered relevant variable and τ_{a} is generally nonlinear, that invalidate the average shear stress as an effective describing parameter. Hence, it is required to understand the fluctuation component of τ_{a}' defined as

$$\tau_{\mathrm{a}}'(x,\,t) = \tau_{\mathrm{a}}\,(x,\,t) - \bar{\tau}_{\mathrm{a}}(x), \qquad (1)$$

and how it varies statistically with flow condition.

The fluctuation of aerodynamic wall shear stress in pure fluid has been widely studied. In classic approaches, the statistics of $\tau_{\mathrm{a}}'/\bar{\tau}_{\mathrm{a}}$ was considered to be constant with the Reynolds number [7]. However, recent investigations have shown that the Reynolds number affects $\tau_{\mathrm{a}}'/\bar{\tau}_{\mathrm{a}}$. It was found that a very large instantaneous value above $\bar{\tau}_{\mathrm{a}}$ that can reach 6 times the mean value [8]. Such a large amplitude of fluctuation is important in several applications, for example, the burst releasing of ground sand particles [9]. The nonlinear interaction between the eddies causes a departure from Gaussian behavior in the probability density function of τ_{a}', which is always positively skewed with skewness ranging from 0.5 to 1.14 [10–16]. In wall-bounded turbulent flow, large-scale and quasi-coherent motion is a fundamental feature which is partially responsible for the production and dissipation of the turbulence in the boundary layers [11]. The evidence that quasi-coherent structures exist is the correlation between the fluctuating velocity and wall shear stress [17]. The large-scale and very large-scale structures has been verified in all types of wall-bounded flow [18,19]. These large-

[a] e-mail: hew15@lzu.edu.cn
[b] e-mail: zhang-j@lzu.edu.cn (corresponding author)

Table 1 List of variables

Symbols	Description	Unit
A_i	Opening area of sand trap	m^2
B	Fitting parameter of the hot-film sensors	–
c	Thickness of sand bed	m
d_P	Particles diameter	$\mu\mathrm{m}$
e_0	Output signal of hot-films in motionless air	–
e_w	Output signal of hot-films with airflow	–
f_H	Sampling frequency of the hot-film sensor	Hz
q	Sand mass flux	$\mathrm{kg/(m^2.s)}$
q^+	Sand mass flux normalized by $\sum q$	–
R	Correlation coefficient	–
Re_∞	Reynolds number of incoming wind velocity	–
Re_τ	Reynolds number of skin friction velocity	–
t	Time coordinate	s
t^+	Normalized time $(t \times f_H)$	–
x, y, z	Streamwise, spanwise, and vertical coordinates	m
$\Delta x, \Delta y, \Delta z$	Streamwise, spanwise, and vertical distance between two hot-film sensors	m
U_∞	Incoming wind velocity	m/s
$\bar{U}$	Mean wind velocity	m/s
U^+	Wind velocity normalized by u_τ	-
u_τ	Skin friction velocity	m/s
$\bar{u}_\tau$	Mean skin friction velocity	m/s
u_c	Convection velocity of near-wall turbulent structures	m/s
f^+	Normalized frequency $(f^+ = fc/U_\infty)$	
z_H	Thickness of hot-film sensors	$\mu\mathrm{m}$
$L(t)$	Gaussian white noise	$\mathrm{m/s}^2$
γ	Damping constant	1/s
$\hat{\sigma}$	Strength of Gaussian white noise	–
β	Local relaxation $(\gamma/\hat{\sigma}^2)$	1/s
T_U	Large time scale of the fluctuation of β	–
δ^*	Thickness of boundary layer	m
δ	A given Time scale to calculate velocity difference	–
Δu_t	Local friction velocity difference	m/s
Δu_s	Spatio-friction velocity difference	m/s
U_t	Normalized local friction velocity difference $[(\Delta u_t - \bar{\Delta u_t})/\sigma_{\Delta u'_t}]$	–
U_s	Normalized spatial friction velocity difference $[(\Delta u_s - \bar{\Delta u_s})/\sigma_{\Delta u'_s}]$	–
E	Relaxation dynamic of Δu	-
E_1	Linear relaxation dynamic of Δu_t and Δu_s	–
E_2	Three-order relaxation dynamic of Δu_t and Δu_s	–
ϵ	Local energy dissipation rate	$\mathrm{m^2/s}^3$
τ_a	Aerodynamic shear stress	$\mathrm{N/m}^2$
τ_a'	Fluctuation of τ_a $(\tau_\mathrm{a} - \bar{\tau}_\mathrm{a})$	$\mathrm{N/m}^2$
$\tau_\mathrm{a}'^+$	Normalized fluctuation of τ_a $(\tau_a'/\bar{\tau}_a)$	–
$\tau_\mathrm{a,std}$	Standard deviation of τ_a	$\mathrm{N/m}^2$
$\tau_\mathrm{a,rms}$	Root mean square of τ_a'	$\mathrm{N/m}^2$
I_τ	Magnitude of fluctuation in τ_a $(\sqrt{\langle \tau_\mathrm{a}'^{+2} \rangle})$	–
ρ_a	Density of the air	$\mathrm{kg/m}^3$
ρ_p	Particle density	$\mathrm{kg/m}^3$
ν	Kinematic viscosity of air	$\mathrm{N.m/s}^2$

scale structures influence near-wall flow fluctuation significantly via superposition and amplitude modulation [20–22]. To grasp the most important statistics properties from this superposition and modulation dynamic, a superstatistics realization was put forward to construct stochastic differential equations with spatio-temporally fluctuating parameters [23]. This realization has been widely used in analyzing the Euler and Lagrangian turbulence flows [24–26].

The majority of past studies have focused on fluctuation of aerodynamic wall shear stress in fluid flows without particle-laden, only a handful of research has been made in particle-laden flows [27–31]. For the past few years, scientists began to realize the effects of the

fluctuation in aerodynamic wall shear stress on particle saltation in boundary layer [27]. Research examined the sand-laden flow and found that aerodynamic wall shear stress exhibits variability over a wide range of timescales due to turbulent mixing aloft [28–31]. They found that the saltation in wind-sand flow is always intermittent, which cannot be predicted by the averaged aerodynamic wall shear stress. Therefore, direct measurement of τ_a in sand-laden flow is essential for understanding the mechanism of intermittent saltation. However, there are some challenges. Direct measurement of τ_a in sand-laden flow is difficult because sand particles can damage frail sensors, especially in high Reynolds number flows in which saltating particles have higher speed. Direct numerical simulation can overcome these problems but remains limited to flows with low Reynolds numbers [32]. Up to now, a direct measurement of aerodynamic wall shear stress in particle-laden flow is still rare, that becomes a huge constraint on the development of relevant research and motivates us to carry out the work of this paper.

In this study, we firstly used flush-mounted hot-film aerodynamic wall shear sensors fabricated with an improved technique to measure τ_a in a sand-laden wall-bounded turbulent flow [33]. Table 1 lists all variables used in this paper. Our aim was to understand the features of τ_a in a sand-laden flow of a simulated turbulent boundary layer in wind tunnel. Our findings improve the current state of knowledge and help address the following key knowledge gaps pertinent to wall shear modulation by airborne sand particles:

- Differences between statistical properties of τ_a in sand-free and sand-laden flows, including the probability density and turbulent intensity of τ_a';
- Modulation of the convective velocity and power spectra from airborne sand particles;
- Superstatistical (SS) analyses of τ_a and the spatio-temporal fluctuation of turbulent energy dissipation rate.

2 Methodology

2.1 Experimental setup and materials

Our experiments were conducted in the wind tunnel at Lanzhou University, China. The wind tunnel simulates well turbulent flow in the near-wall region [34]. The working section of the wind tunnel is $1.3 \times 1.45 \times 22\,\mathrm{m}^3$ (Fig. 1a, coordinates for the streamwise, spanwise, and vertical directions are X, Y and Z, respectively). The incoming wind velocities (U_∞) are 9.28 , 13.26 and 17.41 m/s. We used spires and roughness elements to generate the turbulent boundary layer. Three identical spires were installed at the inlet of the working section with a transverse distance of 0.4 m. The spires were followed by a 6 m streamwise array of roughness elements covering about 50% of the floor surface. The sand bed started 7.5 m downstream of the trailing edge of the roughness

element section. At this position, the simulated atmospheric boundary layer was fully developed. Sand particles from the Tengger Desert of China were used to generate a sand bed 4 m long, 1 m wide, and 0.03 m thick. The lognormal distribution of the diameter of sand particles is presented in Fig. 1c. The sand bed was followed by a 14 cm streamwise fetch of hot-film sensors. To prevent the sensors from becoming buried in the sand, we left a 0.5 m gap between the sand bed and the sensor array. A pitot probe was set at the front of the wind tunnel to measure the incoming wind velocity. A group of pitot probes was used to measuring wind velocity. A sand trap was installed after the hot-film sensors to measure the sand flux. The flush-mounted hot-film sensors were fully flexible and thin (Thickness $z_H = 80\,\mu\mathrm{m}$). A hot wire 1 mm long on the top of the flexible element was the key component of the sensor. The sampling frequency of the sensor was set to 2 kHz (f_H), and the sampling error was within $\pm 5\%$ [35]. To measure the spatial distribution of aerodynamic wall shear stress and to avoid the interplay between sensors, we arranged the hot-films in an array as shown in Fig. 1d. The ratio of hot-film thickness to viscous sublayer thickness was less than 0.3.

2.2 Incoming wind velocity and hot-film calibration

Profiles of the normalized mean velocity ($U^+ = \bar{U}/u_\tau$) of three incoming winds are shown in Fig. 2a. The averaged friction velocity ($\bar{u}_\tau$) was calculated from a logarithmic fit:

$$U(z) = \frac{\bar{u}_\tau}{\kappa}\ln(\frac{z}{z_0}), \qquad (2)$$

where $\kappa = 0.41$ and z_0 is the roughness height. The voltage output of hot film can be converted into wall shear stress with the following equation:

$$(\bar{\tau}_a)^{1/3} = \mathrm{B}\frac{e_0 - e_w}{e_0}, \qquad (3)$$

where e_0 is the voltage in the motionless air, e_w is the voltage with air moving past the sensor, and B is a fitting parameter. The wall shear stress used to calibrate the hotfilms was obtained by $\bar{\tau}_a = \rho_a \bar{u}_\tau^2$. The calibration results of 12 hot-film sensors (four of which were damaged by sand) are presented in Fig. 2b.

2.3 Accuracy analysis of hot-films

The hot-film works based on the principle of thermal balance, that requires us to determine the accuracy of the sensors and how much the sand particles in the wind-blown sand flow will interfere with the measurement signal of the hot-film sensor. Figure 3a shows the profiles of Reynolds stress measured by a two-component hot-wire anemometer. The skin friction velocities were determined by the peak of $\overline{u'w'}$ curves [36] and plotted in Fig. 3b, which shows good
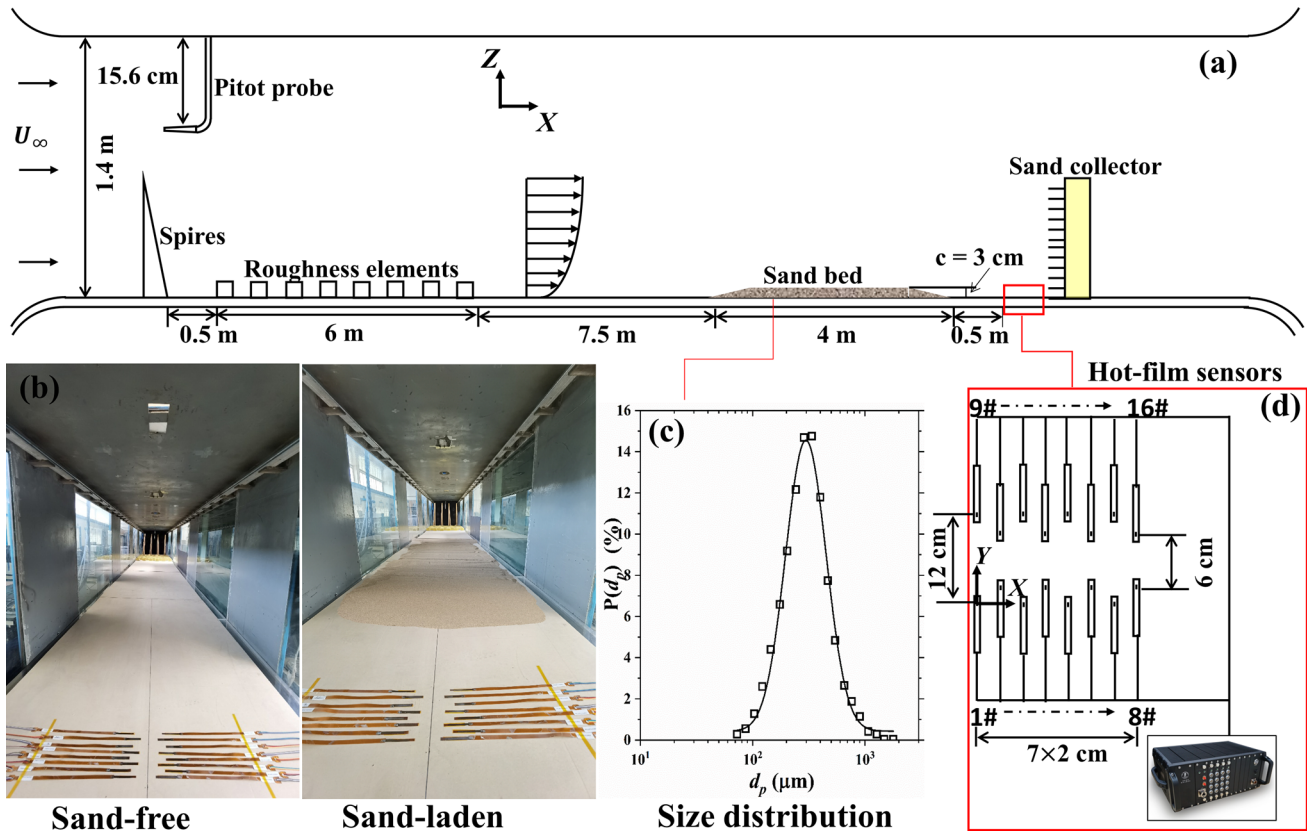
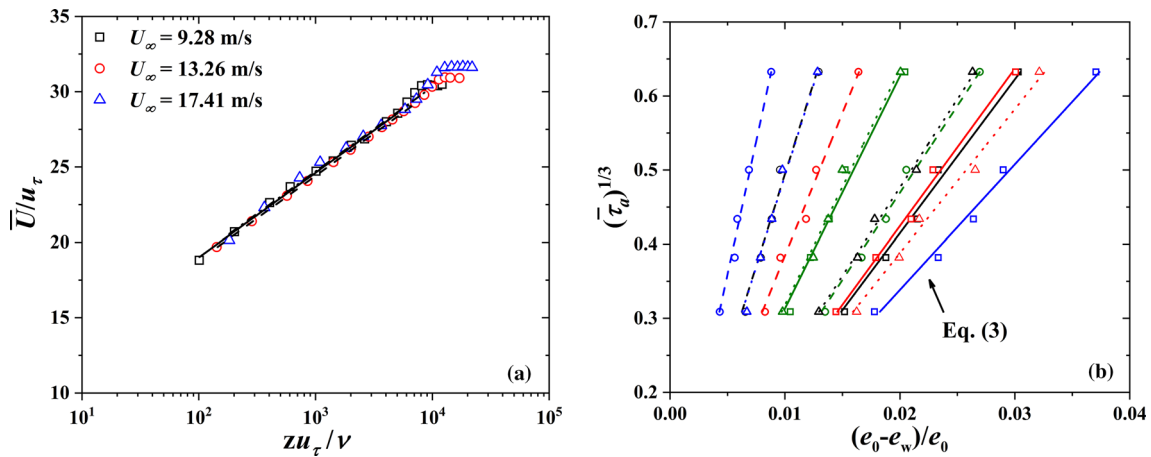**Fig. 1** The experimental setup in the wind tunnel

Fig. 2 a Profiles of mean wind velocity ($\bar{U}/u_\tau$) in three simulated atmospheric boundary layers, the dots indicate the results measured by Pitot tube, and the line is a theoretical logarithmic profile. **b** Calibration of the hot-film sensors

agreement between the hot-film data and hot-wire measurement. Deviations of $0.7 - 6.6\%$ were found between hot-film and hot-wire sensors within the measurement range.

To estimate the strength of noise introduced by sand bombardment, sand particles were used to hit a hot-film sensor directly in motionless air. As shown in Fig. 4a, an intuitive comparison between the noise of bombardment and signal in airflow indicates that the former one is rather weak. Figure 4b shows that the strength

of the bombardment noise is about one order of magnitude lower than signal in airflow corresponding to three incoming wind velocities.

2.4 Vertical profile of the sand mass flux

The sand flux was measured with a sand trap. Each collector had a $2 \times 2 \, \text{cm}^2$ opening that faced the inlet
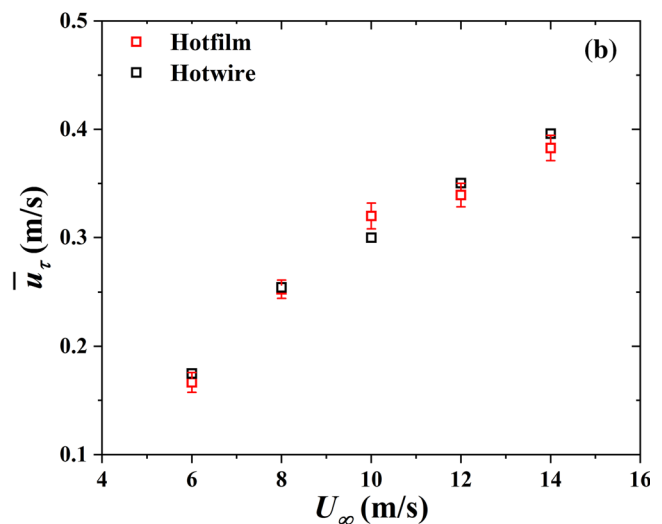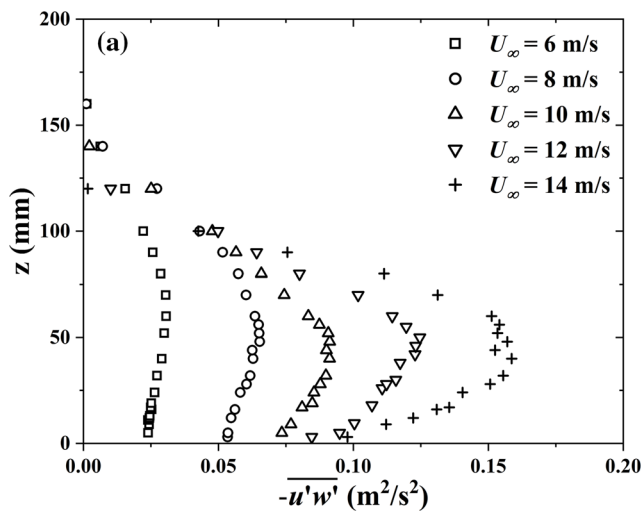
Fig. 3 Accurate analysis of hot-film sensors. **a** Vertical profiles of Reynolds stress with two-component hot-wire anemometry for a wooden wind tunnel floor, and **b** Averaged skin friction velocity $\bar{u}_\tau$ measured with hot-film sensors and a two-component hot-wire anemometer
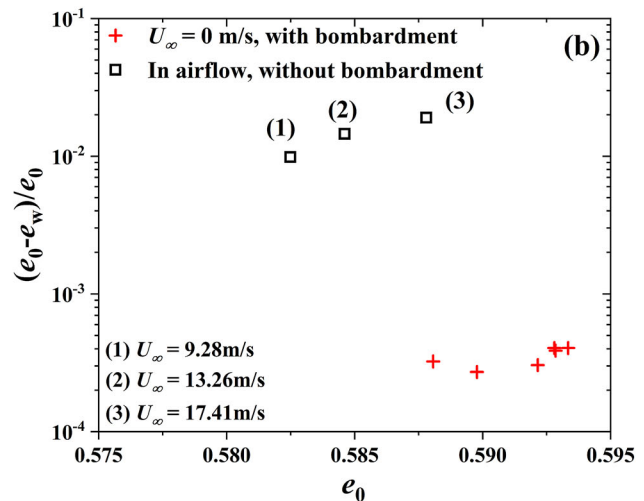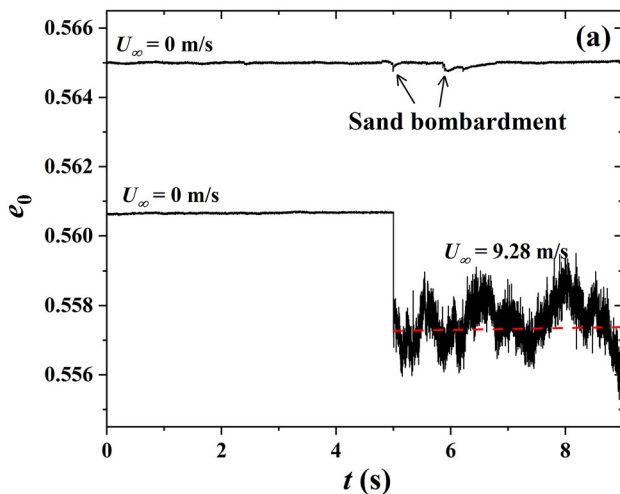

Fig. 4 Estimation of noise strength introduced by particle bombardment. **a** A typical noise signal of particle bombarding a hot-film sensor, and **b** Strength of bombardment noise and average of hot-film signal of three incoming wind velocities used for experiment

wind flow. The sand flux was calculated as

$$q_{\mathrm{i}} = \frac{m_{\mathrm{i}}}{t \times A_i}, \tag{4}$$

where m_{i} is the total mass of sand in ith collector, t is the sampling time, and $A_i = 4\,\mathrm{cm}^2$. Figure 5a shows a comparison between the mass flux measured in a fully developed wind-sand flow [37] and the results of this article. The sand mass flux is normalized by $\sum q$ to remove the effects from different incoming wind velocities. The normalized sand mass fluxes show a decrease as z/c increasing, but the flux profiles measured in our experiment is distinguished from the results of Ref [37]. Our measurements show lower magnitude of sand mass flux in the near wall region, and higher sand mass flux of mid to high positions ($z^+ = 2 \sim 8$). This discrepancy is caused by the difference of particle–surface interac-

tion process over sand and wood surface. Over our wood surface, the bed particles are absent and the fall-down particles have no chance to eject particles moving close to the surface but will get higher rebound velocity (compared to the condition of sand bed) to leads to higher sand mass flux of mid to high positions. Figure 5b illustrates a comparison between the measured results and the predictions of Bagnold's equation [38], Kawamura's equation [39] and Duran's equation [40] for the rate of streamwise sand transport per unit width (Q) in saturated wind-sand flow. It is found that the sand transport in this paper is not saturated. In addition, the magnitudes of Q for three incoming wind velocities are listed in Table 2.

Table 2 gives a summary of the experimental condition, where the characteristics scales used to determine Re_∞ and Re_τ are half of the wind tunnel height and the
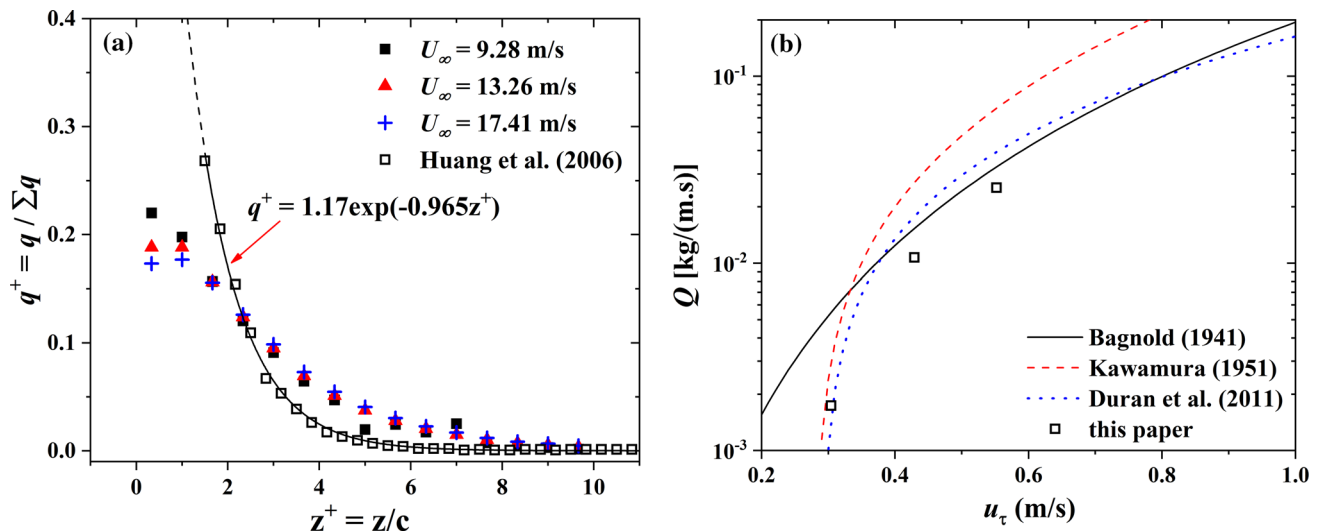
Fig. 5 **a** Comparison between the normalized sand mass flux in this article and the experiment data from a fully developed wind-sand flow, and **b** Comparison of the measured results with the predictions of Bagnold's equation, Kawamura's equation and Duran's equation for the rate of streamwise sand transport per unit width and unit time in saturated wind-sand flow

Table 2 Incoming flow conditions for **a** sand-free flow. **b** sand-laden flow

a

U_∞ (m/s)	δ^* (m)	Re_∞	$\bar{\tau}_a$ (Pa)	$\tau_{a,std}$ (Pa)	Re_τ	
9.28	0.45	3.99×10^5	0.118	0.044	0.91×10^4	
13.26	0.4	5.71×10^5	0.233	0.088	1.14×10^4	
17.41	0.4	7.49×10^5	0.386	0.151	1.46×10^4	

b

U_∞ (m/s)	c (m)	Re_∞	$\bar{\tau}_a$ (Pa)	$\tau_{a,std}$ (Pa)	Re_τ	Q [kg/(m.s)]
9.28	0.03	3.99×10^5	0.109	0.056	0.86×10^4	0.00174
13.26	0.03	5.71×10^5	0.190	0.103	0.99×10^4	0.01073
17.41	0.03	7.49×10^5	0.337	0.187	1.33×10^4	0.02536

thickness of boundary layer, respectively. In addition, the skin friction velocity u_τ that used to calculate Re_τ is determined by $u_\tau = \sqrt{\tau_a/\rho_a}$.

3 Results

3.1 Characteristics of fluctuation in aerodynamic wall shear stress

3.1.1 Time series and probability distribution of τ_a

Figure 6 gives an example of fluctuation in aerodynamic wall shear stress. A high degree of correlation among the four streamwise mounted hot-film sensors can be observed, which indicates the existence of a streamwise footprint in the near-wall region. The time history of τ_a is characterized by the frequent occurrence of large-magnitude positive peaks. However, negative peaks of a similarly large magnitude are rare. The statistics

parameters (Table 2) show that the fluctuation of τ_a in the sand-laden flow increases slightly compared to the sand-free flow, indicating airborne sand particles enhance the fluctuation in τ_a. But the mean fluid shear stress ($\bar{\tau}_a$) is decreased in the sand-laden flow compared to the sand-free flow.

3.1.2 Intensity of fluctuation in τ_a

Figure 7 shows the turbulent intensity in τ_a ($I_\tau = \sqrt{\langle\tau_a'^{+2}\rangle}$) as a function of the Reynolds number, which indicate the effects of Reynolds number on I_τ [41]. Also presented in this figure are data for a zero-pressure-gradient turbulent boundary layer from Ref. [32,42–44]. The Reynolds trend of I_τ in the sand-free flow is similar to Mathis 's result [32], which reported that I_τ increases gradually with the Reynolds number. Our experimental results can be fitted by Mathis's logarithmic formula with same slope: $I_\tau = 0.217 + 0.018\ln(Re_\tau)$. The slope of I_τ is much steeper in the sand-laden flow than in the sand-free flow, which indicates that I_τ increases rapidly

Fig. 6 Time history of $\tau_a'/\bar{\tau}_a$ in the streamwise direction in the sand-free flow and sand-laden flow, $\text{Re}_\infty = 3.99 \times 10^5$
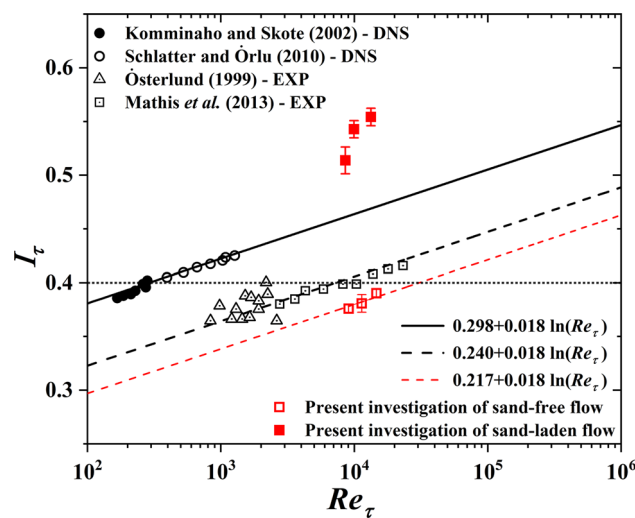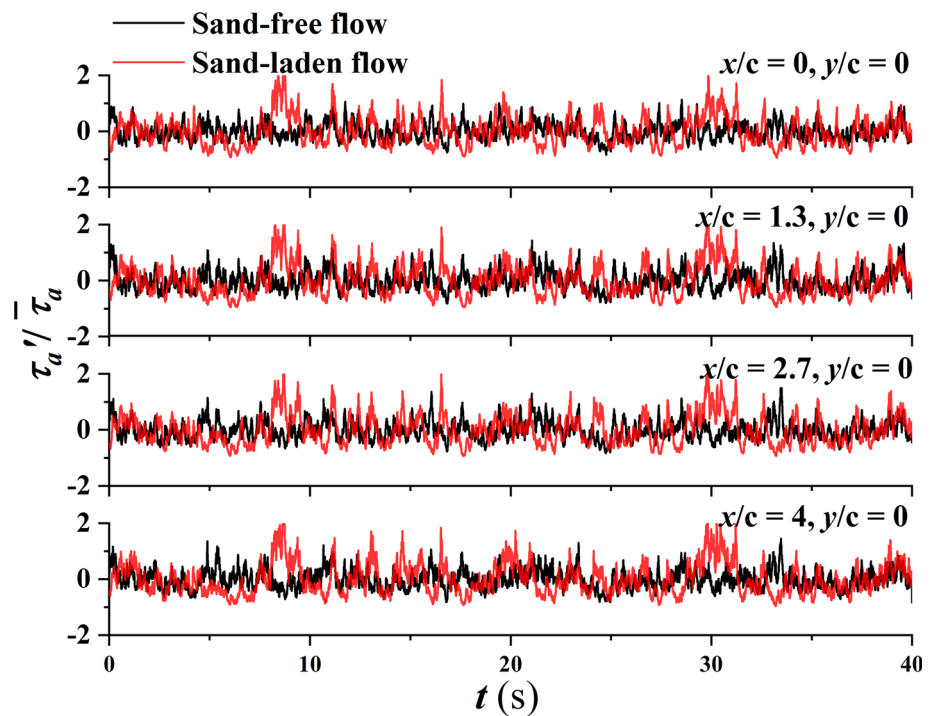

Fig. 7 Turbulent intensity of τ_a versus Reynolds number (Re_τ) for the predictions and available data for sand-free and sand-laden flows. The solid line indicates the trend in Reynolds number reported in Ref. [44], the black dashed line indicates the trend in Reynolds number reported in Ref. [32], and the red dashed line indicates the trend $I_\tau = 0.217 + 0.018\ln(\text{Re}_\tau)$. The horizontal point line marks the classical value of 0.4 suggested in Ref. [10]
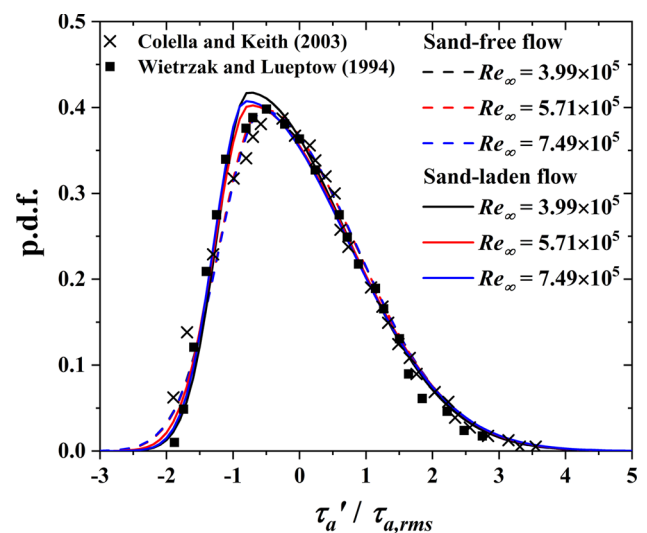
Fig. 8 The probability density function (p.d.f) of normalized fluctuation in aerodynamic wall shear stress ($\tau_a'/\tau_{a,\,\text{rms}}$) for several Re_∞ in the sand-free and sand-laden flows compared to other investigations

with the sand mass flux. Furthermore, the turbulent intensity in aerodynamic wall shear signals is more sensitive to the increase in the sand mass flux than the Reynolds number.

Figure 8 shows the probability density function (p.d.f) of $\tau_a'/\tau_{a,\,\text{rms}}$ for $\text{Re}_\infty = 3.99 \times 10^5$, 5.71×10^5 and

7.49×10^5, where $\tau_{a,\,\text{rms}}$ is the root mean square of τ_a'. Our data for all Reynolds numbers in the sand-free flow are consistent with the results of Colella and Keith [11] and Wietrzak and Lueptow [12]. The skewness and flatness of the six curves presented in Fig. 8 are listed in Table 3c. Also included in the table are experimental results for flush-mounted hot-element sensors and elevated hot-element wall shear sensors from the literature. The addition of

Table 3 Wall shear fluctuation measured by different types of sensors

Type of sensor	I_τ	Skewness	Flatness	Flow condition
(a) Flush-mounted hot-element wall shear sensors				
Glue-on gauge wall shear stress probe (DANTEC 55R47, [13])	0.123	0.61	3.45	Turbulent air boundary layer, $Re_\theta = 2700$
Hot-film sensors used in an oil channel flow	0.4	1.1	5.0	Turbulent oil channel flow, $Re_d = 3800$
Quartz-substrate gauge wall shear stress probe (DISA 55R45, [10])	0.095	0.5	3.3	Turbulent air boundary layer flow, $Re_\delta = 3800$
Flush-mounted hot-film [14]		0.53	3.1	Turbulent air duct flow
(b) Elevated hot-element wall shear sensors				
2 μm diameter wire placed a few diameters away from a Plexiglas plug [10]	0.39	1.0	4.8	Turbulent air boundary layer flow, $Re_\delta = 28,000$
Marginally elevated 5 μm diameter hot wire 85 μm from a Perspex wall substrate [15]	0.32– 0.39 (≈ 0.38)	0.75– 1.25 (≈ 1.14)	3.6–5.2 (≈ 4.7)	Turbulent air boundary layer flow, $Re_\delta = 20,000 - 460000$
Flush-mounted hot wire wall shear stress probe [16]	0.23–0.29			Turbulent air channel flow with Re_d ranging from 3300–33,000

U_∞ (m/s)	I_τ	Skewness	Flatness	Flow condition
(c) Wall shear fluctuation in the present investigation				
9.28	0.376 ± 0.04	0.47-0.80 (≈ 0.61)	3.10-4.05 (≈ 3.52)	TBL, $Re_\infty = 3.99 \times 10^5$
13.26	0.381 ± 0.08	0.58-0.88 (≈ 0.66)	3.51-4.31 (≈ 3.69)	TBL, $Re_\infty = 5.71 \times 10^5$
17.41	0.390 ± 0.04	0.47-0.87 (≈ 0.61)	3.13-4.44 (≈ 3.52)	TBL, $Re_\infty = 7.49 \times 10^5$
9.28	0.514 ± 0.13	0.80-1.04 (≈ 0.92)	3.63-4.91 (≈ 4.25)	TBL with sand-laden, $Re_\infty = 3.99 \times 10^5$, $Q = 0.00174$
13.26	0.543 ± 0.08	0.57-1.07 (≈ 0.81)	3.05-4.56 (≈ 3.81)	TBL with sand-laden, $Re_\infty = 5.71 \times 10^5$, $Q = 0.01073$
17.41	0.554 ± 0.08	0.71-1.16 (≈ 0.90)	3.42-5.40 (≈ 4.04)	TBL with sand-laden, $Re_\infty = 7.49 \times 10^5$, $Q = 0.02536$

sand particles increases the skewness of the p.d.f. That is, airborne sand particles enhance the large-scale positive peaks in the time history of wall shear fluctuation.

3.1.3 Convective velocity u_c

To determine the convective velocities u_c of the streamwise τ_a fluctuations in the boundary layer with and without sand-laden, data of two hot-film sensors separated by a streamwise distance of Δx were employed. The time-averaged correlation between two hot-film sensors is defined as

$$R_{\tau'_{a,1}\tau'_{a,2}}(\Delta t) = \frac{\overline{\tau'_{a,1}(t,x)\tau'_{a,2}(t+\Delta t, x+\Delta x)}}{\tau'_{a,1}(x)_{rms}\,\tau'_{a,2}(x+\Delta x)_{rms}}, \quad (5)$$

where $\tau'_{a,1}$ and $\tau'_{a,2}$ are the streamwise fluctuation in shear stress of airflow, respectively, and Δt is the time delay. Correlations were averaged over sampling periods in multiples of 5 s and normalized with the root mean square (r.m.s) to eliminate uncertainty from calibration.
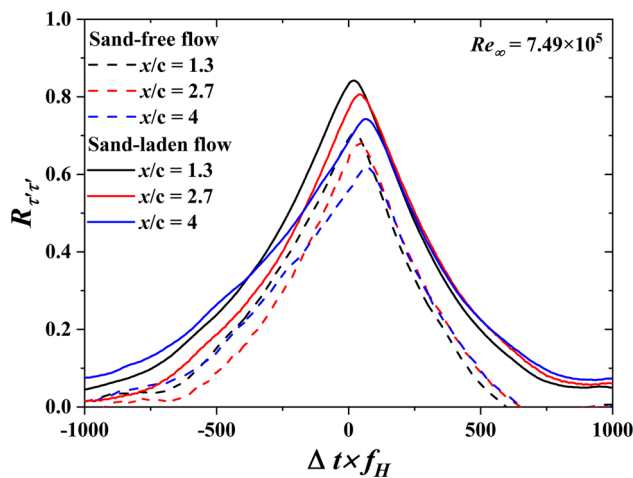
Fig. 9 Correlation of aerodynamic wall shear fluctuation $(R_{\tau'_{a,1}\tau'_{a,2}})$ with several streamwise intervals in sand-free and sand-laden flows

Figure 9 shows correlations between τ'_a, in which the time delay is pre-multiplied by the frequency of the wall shear sensor. The decrease in the correlation coefficient with the increasing interval between two wall shear sensors is consistent with the decay in the structures as they move along the streamwise direction. The maximum of correlation curves is higher in the sand-laden flow than the sand-free flow. Furthermore, it takes longer for the correlation curve to decrease to zero compared to the sand-free flow, which indicates a larger integral time scale in sand-laden flow.

As Δx increases, the peaks of the correlation curves shift toward time delays with larger values. In Fig. 10a, the normalized time shift ($\Delta t U_\infty/c$), where the peak of the correlation curve occurs, is plotted against the normalized streamwise distance ($\Delta x/c$, where c is the thickness of the sand bed). The time shift increases approximately linearly with the streamwise separation distance within the range of scatter, which indicates

the existence of a constant convective velocity of u_c. The results of u_c for various incoming wind velocities with and without sand-laden are plotted in Fig. 10b. In sand-laden flow, u_c are 6.7, 2.5 and 6.5% lower as compared to the sand-free flow, which indicates slower streamwise movement of near-wall turbulent structures.

3.1.4 Spectra of aerodynamic wall shear stress

Following Newland [45], we calculated the power spectral density function from a fast Fourier transform with a rectangular spectral window. Figure 11 shows the normalized spectra of aerodynamic wall shear stress at four streamwise positions. The distinction between spectral distributions at different positions is not clear. In the sand-free flow, the peak of the spectra is at $fc/U_\infty = 1.4 \times 10^{-3}$ and is followed by several slightly lower peaks. In the sand-laden flow, peaks of the spectra are at $fc/U_\infty = 0.62 \times 10^{-3}, 1.7 \times 10^{-3}$ and 2.9×10^{-3}. These peaks are outstanding compared with sand-free flow.

Figure 12 shows the power spectral density in the sand-free and sand-laden flows with different incoming wind velocities. To minimize possible error caused by different sensors, we averaged the power spectra of 12 sensors. In the sand-laden flow, there is more energy at lower frequencies, indicating the enhanced large turbulence in the near-wall region. In a field observation, Baas and Sherman [46] found a high concentration of windblown sand elongated in the streamwise direction. This phenomenon was defined as aeolian streamers and successfully simulated by Dupont et al. [47]. In the sand-laden flow, the sand concentration field and streamwise wind velocity appear to be anti-correlated in the near-wall region ($z \leq 0.1z_m$, where z_m is the height of the saltation layer), and high concentration is correlated with low wind velocity. They explained this anti-correlation in terms of the momentum extracted from the flow by the sand particles. The lifetime of streamers is on the order of 1.0 s (about 1 Hz sig-
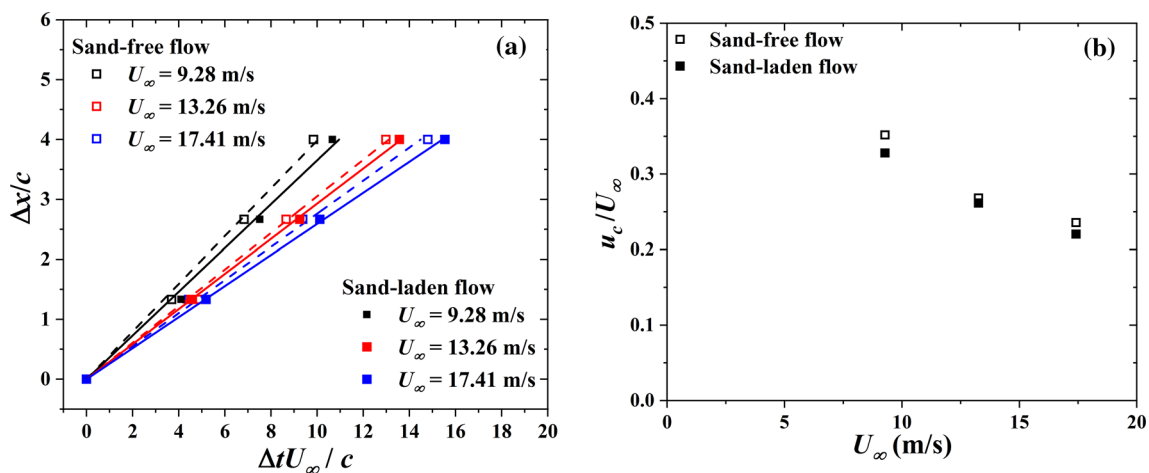

Fig. 10 a Time shift of maximum correlation as a function of streamwise distance ($\Delta x^+ = \Delta x/c$), **b** Convective velocity u_c for different values of incoming wind velocities in sand-free and sand-laden flows, respectively
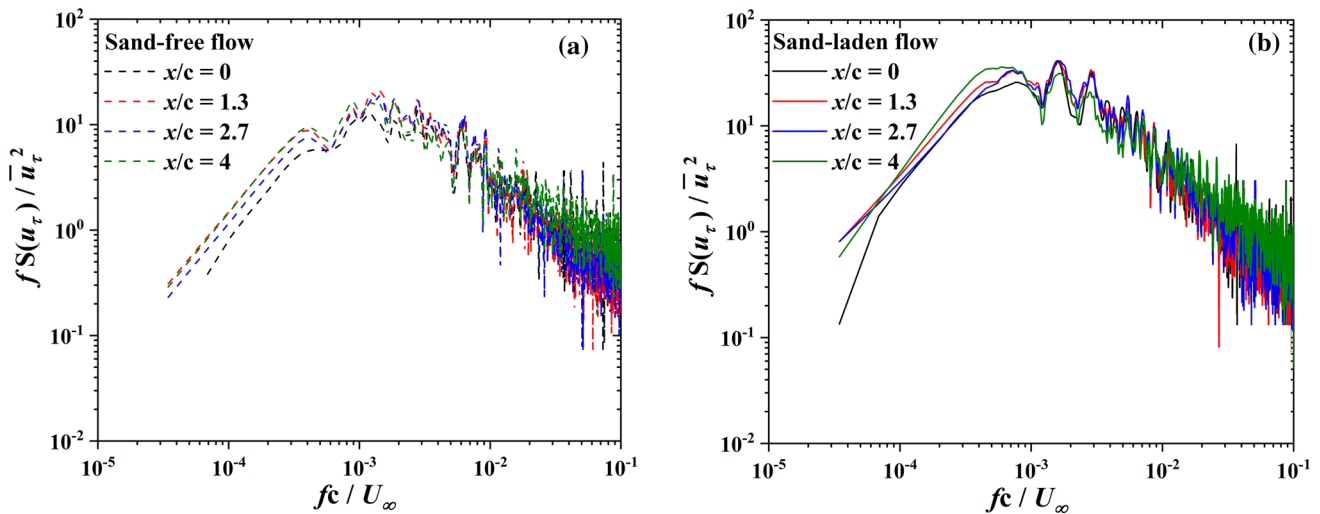
Fig. 11 Normalized power spectral density of streamwise skin friction velocity fluctuation $\left(fS\left(u_\tau\right)/\bar{u}_\tau^2\right)$ at several positions in the sand-free (a) and sand-laden (b) flows. The incoming wind velocity is $U_\infty = 17.41\,\mathrm{m/s}$
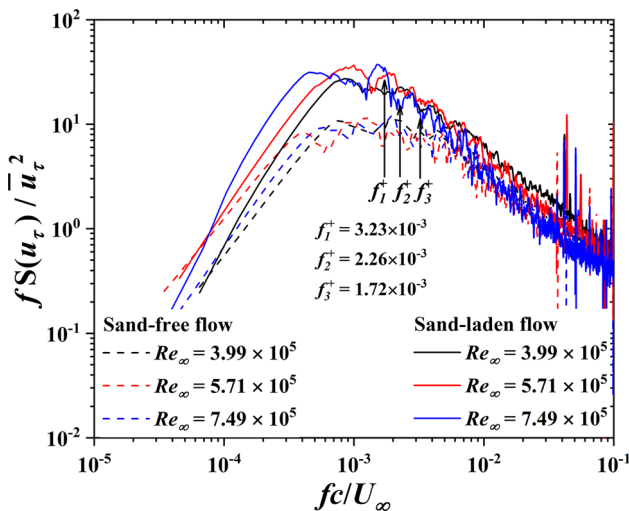

Fig. 12 Normalized power spectral density of streamwise skin friction velocity fluctuation $\left(fS\left(u_\tau\right)/\bar{u}_\tau^2\right)$ in the sand-free and sand-laden flows

nal). The corresponding normalized frequencies of three incoming U_∞ in this work are 3.23×10^{-3}, 2.26×10^{-3} and 1.72×10^{-3} . All of these normalized frequencies fall into the range of increased power spectra in the sand-laden flow (arrows in Fig. 12). These streamers provide a possible explanation for the extra source of low-frequency signals. Furthermore, the increase in energy at low frequencies suggests an increase in the r.m.s of τ_a'. This is well supported by Fig. 7, which shows that the magnitude of fluctuation (I_τ) increases rapidly with the Reynolds number in the sand-laden flow.

3.2 Superstatistics (SS) analysis of aerodynamic wall shear stress

In this section, we intent to use superstatistics (SS) to grasping the most important statistical properties of

aerodynamic wall shear fluctuation and to analyze the effects of airborne sand particles on the dynamic of this stochastic system.

In wall-bounded turbulent flow, inner–outer interactions relate to superposition and modulation effects [48]. A simple dynamical realization of this superposition and modulation can be constructed by considering stochastic differential equations with spatio-temporally fluctuating parameters [23]. Consider the Langevin equation:

$$\dot{\Delta u} = \gamma F\left(\Delta u\right) + \hat{\sigma}L\left(t\right), \tag{6}$$

where $\gamma > 0$ is a damping constant, $F\left(\Delta u\right)$ is a drifting force, $L\left(t\right)$ is Gaussian white noise and $\hat{\sigma}$ is the strength of the Gaussian white noise. In turbulent applications, Δu stands for a local velocity difference in the turbulent flow. On a very small time scale, this velocity difference is the acceleration. The basic idea is that Δu locally relax with a damping constant γ and driven by rapidly fluctuation chaotic force difference. To reach a local momentum balance, the chaotic force difference is modeled by Gaussian white noise $L(t)$. If the chaotic force difference acts on a relatively small time scale compared to γ^{-1} and has strong mixing properties, the approximation of Gaussian white noise has been proved to be rigid [5,49].

In turbulent flow, the local energy dissipation rate (ϵ) fluctuates in space and time. In the sample model of Eq. (6), this dissipation process is described by the damping constant γ. Furthermore, the parameter β defined as $\beta = \gamma/\hat{\sigma}^2$ is a simple function of ϵ. For a while, there is a local relaxation (or ϵ) with a value of β, then this parameter changes to a new value, as so on.

Finally, the drifting force $F\left(\Delta u\right)$ defined as $F\left(\Delta u\right) = -[\partial/(\partial\Delta u)]E$. In the turbulent applications, E stands for an effective potential generating the relaxation dynamic of Δu. For example, $E = V\left(\Delta u\right) = 1/2\Delta u^2$ generates a linear relaxation dynamic, whereas other
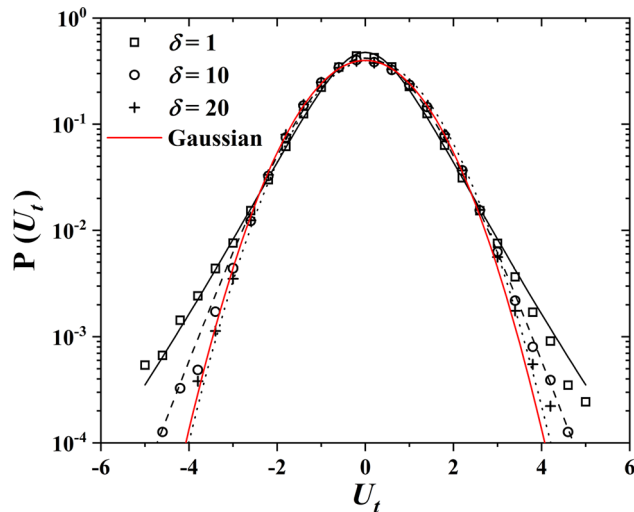
Fig. 13 Probability density function of U_t at several time scales (δ) compared to a Gaussian curve

functions of $V(\Delta u)$ indicate more complicated relaxation dynamics.

3.2.1 SS analysis of local friction velocity difference

With a given time series of skin friction velocity from one shear sensor, the local friction velocity difference, Δu_t, was defined as

$$\Delta u_t = u_\tau \left(t^+ + \delta \right) - u_\tau (t^+), \qquad (7)$$

$$U_t = (\Delta u_t - \overline{\Delta u_t})/\sigma_{\Delta u_t'} \qquad (8)$$

where $t^+ = t \times f_H$, $\sigma_{\Delta u_t'}$ is the standard deviation of $(\Delta u_t - \overline{\Delta u_t})$, and δ is a normalized time scale. The p.d.f of U_t has non-Gaussian behavior at small time scales, which is consistent with Ref. [51]. As shown in Fig. 13,

the experimental data depart from the Gaussian line in small time scales of $\delta = 1$ and 10.

An essential postulating of SS models is the existence of an intensive parameter β that fluctuates on a large spatio-temporal scale T_U. In fact, β is assumed to reach local equilibrium very fast, i.e., the associated relaxation time τ_U is relatively short as compared to T_U. To extract these time scales, U_t is divided into N equal slices of size Δ. The large time scale T_U equals to the length of the slices, and the small time scale τ_U determines how fast the local equilibrium is reached in each slice. We then define a function k_Δ as follows [52]:

$$k_\Delta = \frac{1}{N} \sum_{l=1}^{N} \kappa_{\Delta,l}, \text{ with } \kappa_{\Delta,l} = \frac{\langle U_t^4 \rangle_{\Delta,l}^2}{\langle U_t^2 \rangle_{\Delta,l}}, \qquad (9)$$

$$\langle U_t^i \rangle_{\Delta,l} = \frac{1}{\Delta} \sum_{i=1+(l-1)\Delta}^{l\Delta} U_t^i, \text{ with } l = 1, 2, \ldots, N. \qquad (10)$$

Figure 14a shows k_Δ as a function of Δ. The relevant large time scale T_U is defined by the condition $k_\Delta = 3$. The short time scale τ_U can be estimated from the exponential decay in the correlation function $C_U(t^+) = \langle U_t(t^+)U_t(t^+ + \Delta t^+) \rangle$. As shown in Fig. 14b, the short time scale τ_U is defined by $C_U(\tau_U) = e^{-1}C_U(0)$. These two basic time scales τ_U and T_U are listed in Table 4. The ratios between T_U and τ_U are relatively large, which indicates that the two time scales are well separated. In the sand-laden flow, the value of T_U is decreased compared to the sand-free flow. Generally speaking, for a while, β reaches a local relaxation with a value of $\beta = \gamma/\hat{\sigma}^2$, then this parameter changes to a new value, as so on. As for sand-laden flow, reduced T_U indicates that the changing of β is faster than in sand-free flow.

Then, the slowly varying stochastic process β is calculated in each slice whose length equals T_U. On the time scale T_U, the local stationary distribution in each cell is Gaussian. The variance in local Gaussians
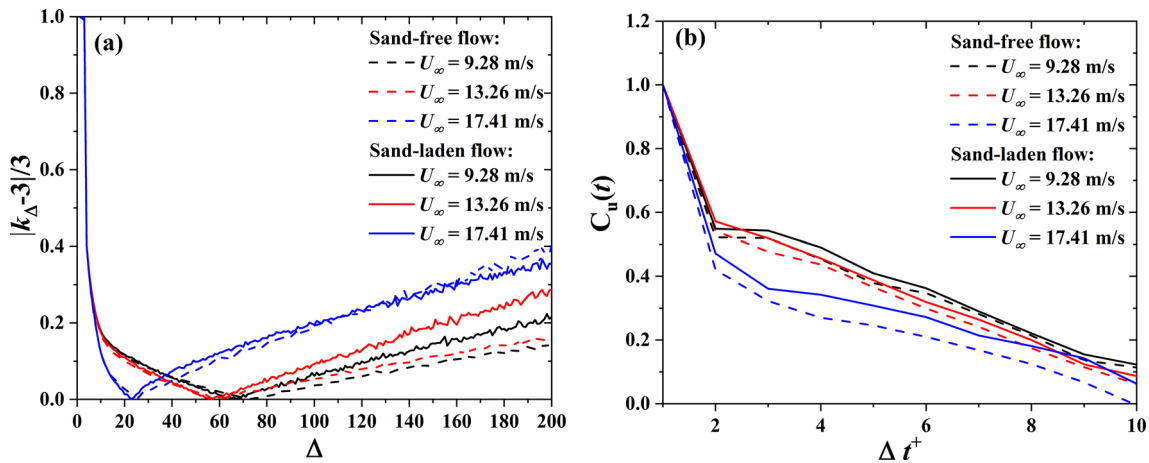

Fig. 14 (a) Determination of the large time scale T_U under the condition $k_\Delta = 3$ for six data series of U_t. **b** Determination of the short time scale τ_U from the decay in the correlation function $C_U(\Delta t^+)$, where τ_U is obtained from $C_U(\Delta t^+) = e^{-1}C_U(0)$

Table 4 Values of superstatistical parameters extracted from the time history of U_t

U_∞ (m/s)	Flow medium	τ_U	T_U	T_U/τ_U	α	θ
9.28	Sand-free	5.40	72	13.3	0.340 ± 0.001	0.164 ± 0.001
	Sand-laden	5.94	67	11.3	0.407 ± 0.001	0.195 ± 0.002
13.26	Sand-free	5.01	60	12.0	0.372 ± 0.007	0.171 ± 0.009
	Sand-laden	5.29	57	10.8	0.481 ± 0.003	0.255 ± 0.004
17.41	Sand-free	2.54	25	9.8	0.482 ± 0.004	0.256 ± 0.005
	Sand-laden	2.95	23	7.8	0.484 ± 0.003	0.312 ± 0.004
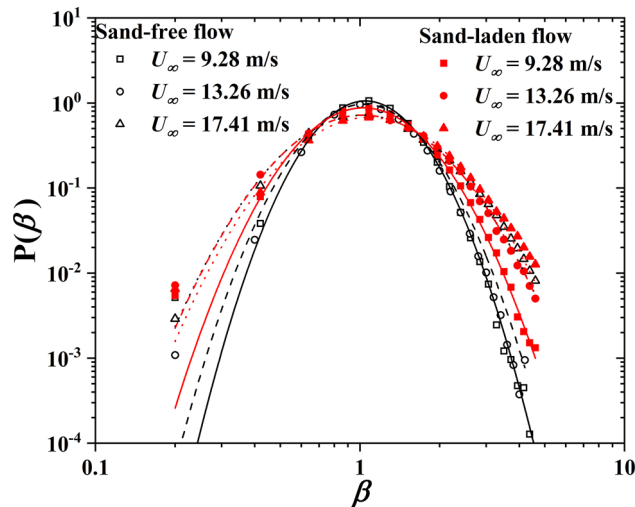
Fig. 15 Probability density function of β in sand-free and sand-laden flows, respectively. The six curves are the log-normal matches of P(β). Parameters α and θ are listed in Table 4

$\sqrt{\beta/2\pi}e^{-1/2\beta U_t^2}$ is given by β^{-1}, and the $\beta(t)$ can be determined according to Ref. [53]:

$$\beta(t) = \frac{1}{\langle U_t^2 \rangle_{t,T_U} - \langle U_t \rangle_{t,T_U}^2}. \quad (11)$$

The p.d.f is obtained from a histogram of $\beta(t)$ for all values of t, as shown in Fig. 15. A good match to the data is the lognormal distribution:

$$f(\beta) = \frac{1}{\alpha\sqrt{2\pi}} \frac{1}{\beta} e^{-\frac{(\ln\beta - \theta)^2}{2\alpha^2}}, \quad (12)$$

with α and θ as listed in Table 4. The log-normally distributed β extracted from U_t indicates that β is a power-law function of the local energy dissipation rate (ϵ) in both sand-free and sand-laden flows. An increase in the standard deviation of β indicates that spatiotemporal fluctuation in the local energy dissipation rate is enhanced by the airborne sand particles.

Finally, we reconstruct $p_{T,f}(U_t)$ as

$$p_{T,f}(U_t) = \int_0^\infty d_\beta f(\beta) \sqrt{\frac{\beta}{2\pi}} e^{-\beta E}, \quad (13)$$

where the subscript T is the length of each slice and f is the frequency. Figure 16 shows both $P(U_t)$ and $p_{T,f}(U_t)$. The SS reconstructions match the experimental data in both sand-free and sand-laden flows.

3.2.2 SS analysis of spatial friction velocity difference

The spatial friction velocity difference is defined as

$$\Delta u_s = u_\tau(x + \Delta x) - u_\tau(x), \quad (14)$$

$$U_s = (\Delta u_s - \overline{\Delta u_s})/\sigma_{\Delta u_s'}, \quad (15)$$

where $\sigma_{\Delta u_s'}$ is the standard deviation of ($\Delta u_s - \overline{\Delta u_s}$), and Δx is the streamwise interval between the two sensors. As the convective velocities u_c are obtained from the correlation peaks of aerodynamic wall shear stress, the time intervals Δt between the two sensors are calculated as $\Delta x/u_c$. The normalized time interval ($\delta = \Delta t \times f_H$) is listed in the insets of Fig. 17. Furthermore, this time interval is substituted into Eqs. (7) and (8) to calculate the p.d.f of U_t and U_s as plotted in Fig. 17.

Then, using the SS approach and the lognormal distribution, which reproduces the fluctuation in β we reconstruct $p_{T,f}(U_t)$ and $p_{T,f}(U_s)$ as

$$p_{T,f}(U_t \text{ or } U_s) = \frac{1}{2\pi s} \int_0^\infty d\beta \exp\left(\frac{-(\ln(\beta/\mu))^2}{2s^2}\right) e^{\beta E}, \quad (16)$$

where $\mu = e^{1/2s^2}$ is due to the variance in U_t and U_s equals 1 [23]. In the sand-free flow, the distributions of $P(U_t)$ and $P(U_s)$ are well predicted by the linear relaxation dynamic $E_1 = (1/2)U_{t \text{ or } s}^2$ (Fig. 17a). However, in the sand-laden flow, $P(U_t)$ and $P(U_s)$ are distinct. These results indicate that Eq. (16) should be modified before it is introduced to the sand-laden flow. As a result, a high-order relaxation dynamic replaces the linear relaxation dynamic in Eq. (16) to generate a better approach to $p_{T,f}(U_s)$. The high-order relaxation dynamic is defined as

$$E_2 = \left(-\frac{1}{2}U_s^2\right) - h \times \left(U_s + \frac{1}{3}U_s^3\right), \quad (17)$$
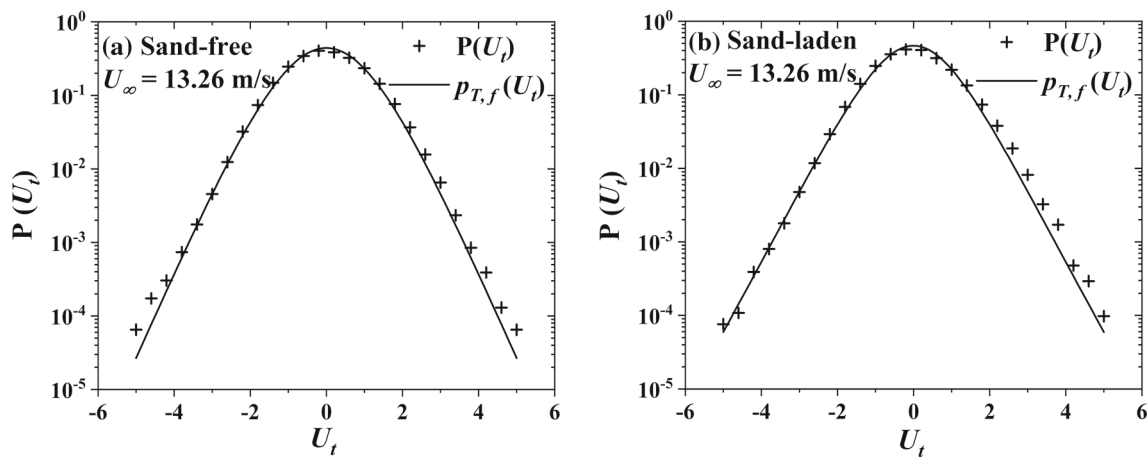
Fig. 16 **a** Probability density of U_t in sand-free and **b** Sand-laden flows. The solid lines represent superstatistical approximations of $p_{T,f}(U_t)$

where h is a constant to be determined. There is good reconstruction of the asymmetry in Fig. 17b. The constants (s, and h) are listed in the insets of Fig. 17.

4 Discussion

For two experiments with and without sand-laden, the magnitude of the fluctuation in aerodynamic wall shear stress increased with increasing Reynolds number, Re_τ (Fig. 7). In the sand-free flow, I_τ increased slowly with Re_τ, which is in agreement with the former results of Refs. [10,32,44]. In the sand-laden flow, I_τ was about 1.4 times as much as that in sand-free flow because the reduced $\bar{\tau}_a$ and enhanced $\tau_{a,\,std}$ (Tab. 2). The decrease in $\bar{\tau}_a$ can be attributed to the transport of momentum to airborne particles. Figure 7 also shows that I_τ is more sensitive to the increase in the sand mass flux than the Reynolds number. However, the mechanism between particle transport intensity and I_τ need further investigations. Figure 8 provides a comparison between p.d.f of τ_a with and without sand-laden. In sand-laden flow, airborne particles enhance the large-magnitude positive peaks occurring with low frequencies (Fig. 6), leading to an increase in skewness of τ_a.

The convective velocity u_c of aerodynamic wall shear fluctuations has been estimated by means of the space-time correlations between τ_a measured by different hot-film sensors (Fig. 9). Based on the time shift of correlation peaks, we obtained u_c of three incoming wind velocities in sand-free and sand-laden flows, respectively (Fig. 10 a). In the presence of sand-laden, this convective velocity is thus about $2.5 - 6.7\%$ lower than in sand-free flow, indicating the blocking effect from airborne particles (Fig. 10 b). Power spectra of skin friction velocities are increased at lower frequencies (Fig. 12). This suggests that the airborne sand particles enhanced the streamwise vortex with larger time scales, which corresponds to the averaged life time of sand streamers visualized in Ref. [47]. Thus, sand streamers provide a possible explanation for the enhanced low-frequency

signals. In addition, the strengthened streamwise vortex with larger time scales leads to enhanced $\tau_{a,\,std}$, which is in agree with the enhanced I_τ in Fig. 7.

Turbulent flow is a system of superposition and modulation which related to inner–outer interactions in the boundary layer. The presence of sand-laden further complicates this stomachic system. By mean of SS technique, we proved that the airborne sand particles reduced the large time scales T_U in which the stomachic system of u_τ difference reaches a local Gaussian distribution (Fig. 14a). In each time scale T_U, the slowly varying stochastic process $\beta(t)$ defines the variance of the local Gaussians. The lognormal distributions of β with and without sand-laden indicate that β is a simple function of local energy dissipation rate of turbulence, ϵ (Fig. 15). In the presence of sand-laden, the variance parameters of β exceed that in the absence of sand-laden, indicating that airborne particles enlarge the temporal difference of ϵ (Table 4). This result provides a proof for the existence of sand streamers which cause significant variation in flow condition near the wall (Ref. [47]).

5 Conclusions

We compared wall shear fluctuation in wall-bounded turbulent sand-free and sand-laden flows. In the sand-free flow, the turbulent intensity of wall shear stress signal increases gradually with the Reynolds number. The turbulent intensity in aerodynamic wall shear stress, I_τ, can be determined by the similar formulas of Ref. [32,44]. In the sand-laden flow, I_τ increases rapidly with the Reynolds number, which indicates that the turbulent intensity in aerodynamic wall shear is more sensitive to sand mass flux than Reynolds number. In the sand-free flow, the positively skewed pdf of $\tau'_a/\tau_{a,\,rms}$ is consistent with classic investigations. However, the increase in skewness indicates that airborne particles in the sand-laden flow enhance the large-scale positively occurring peaks in the time history of τ'_a.
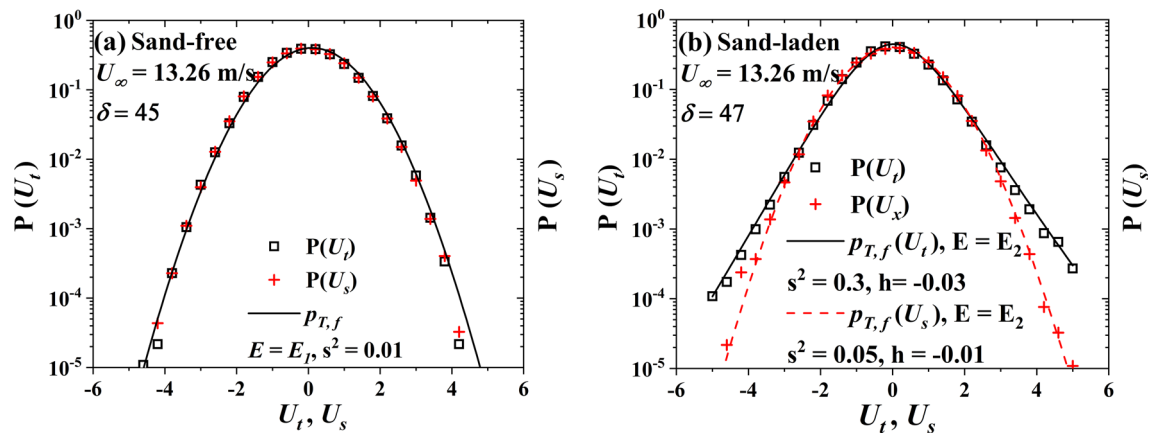
Fig. 17 Probability density of U_t and U_s in the sand-free **a** and sand-laden **b** flows. The dashed lines and solid lines represent superstatistical approximations of $p_{T,f}(U_t)$ and $p_{T,f}(U_s)$, respectively

Correlations between different shear sensors verified the existence of decay in the turbulent structures as they convected along the flow direction. The decrease in the convective velocity in the sand-laden flow indicates slower movement of near-wall turbulent structures due to the blocking effects of airborne sand particles. The wall shear stress spectra of a single sensor show an exponential decrease in the mid-to-high frequencies. In the sand-laden flow, there is an increase in energy at lower frequencies. The frequency range of the enhanced power spectra is consistent with the duration of the sand streamers. Thus, the frequent occurrence of sand streamers explains the enhanced low-frequency signals. Furthermore, the increase in energy at low frequencies also suggests an increase in the r.m.s of τ_a' in the sand-laden flow. This is well supported by Fig. 7, which shows that the magnitude of fluctuation (I_τ) increases rapidly with the Reynolds number in the sand-laden flow.

To extract the two relevant time scales from the wall shear signals, we used the SS method to analyze this non-equilibrated system. As for the local friction velocity difference (U_t), a lognormal distribution was obtained from the parameter β, which is a simple power function of the local energy dissipation rate. In the sand-laden flow, the standard deviation of β is increased by the airborne sand particles, which is consistent with the increased energy at low frequencies. The local and spatio-drifting force acting on the stochastic system of wall shear fluctuation in sand-laden flow are different, providing a proof for the existence of sand streamers which cause significant variation in flow condition near the wall.

The research in this paper has tremendous potential in understanding the mechanism of intermittent saltation in wind-blown sand, which cannot be predicted by the averaged aerodynamic wall shear stress [31].

Author contribution statement

References

1. B. Grant, I. Marusic, Environ. Sci. Technol. **45**, 7107 (2011)
2. O. Durán, P. Claudin, B. Andreotti, Aeolian Res. **3**, 243 (2011a)
3. L. Prandtl, *Motion of Fluids with Very Little Viscosity* (In Verhaldlg III Int. Math, Kong, 1905)
4. H. Schlichting, K. Gersten, *Boundary Layer Theory*, 8th edn. (Springer, NY, 2000)
5. P. Monkewitz, K. Chauhan, H. Nagib, Phys. Fluids **19**, 115101 (2007)
6. B. Khoo, Y. Chew, C. Teo, Exp. Fluids **31**, 494 (2001)
7. A. Smits, B. McKeon, I. Marusic, Annu. Rev. Fluid Mech. **43**, 353 (2011a)
8. R. Örlu, P. Schlatter, Phys. Fluids **23**, 021704 (2011)
9. J. Kok, N. Renno, AGU Fall Meet. Abstr. **43**, 1 (2007)
10. P. Alfredsson, A. Johansson, J. Haritonidis, H. Eckelmann, Phys. Fluids **31**, 1026 (1988)
11. K. Colella, W. Keith, Exp. Fluids **34**, 253 (2003)
12. A. Wietrzak, R. Lueptow, J. Fluid Mech. **259**, 191 (1994)
13. W. Cook, AIAA J. **32**(7), 1464 (1994)
14. K. Sreenivasan, R. Antonia, J. Appl. Mech. **44**(3), 389 (1977)
15. Y. Chew, B. Khoo, G. Li, Exp. Fluids **17**, 75 (1994)
16. D. Shah, R. Antonia, AIAA J. **25**, 22 (1987)

17. J. Cardillo, Y. Chen, G. Araya, J. Newman, K. Jansen, L. Castillo, J. Fluid Mech. **729**, 603 (2013)
18. W. Hambleton, N. Hutchins, I. Marusic, J. Fluid Mech. **560**, 53 (2006)
19. N. Hutchins, I. Marusic, J. Fluid Mech. **579**, 1 (2007a)
20. N. Hutchins, I. Marusic, Philos. Trans. A Math. Phys. Eng. Sci. **365**, 647–64 (2007b)
21. R. Mathis, J. Monty, N. Hutchins, I. Marusic, Phys. Fluids **21**, 111703 (2009)
22. D. Chung, B. McKeon, J. Fluid Mech. **661**, 341 (2010)
23. C. Beck, Physica D **193**, 195 (2004)
24. C. Beck, E.G.D. Cohen, H.L. Swinney, Phys. Rev. E Stat. Nonlin. Soft. Matter. Phys. **72**, 056133 (2005)
25. C. Beck, Rev. Lett. **98**(6), 064502 (2007)
26. H. Xu, N. Ouellette, E. Bodenschatz, Phys. Rev. Lett. **96**(11), 114503 (2006)
27. F. Comola, J. Kok, M. Chamecki, R. Martin, Geo. Res. Lett. **46**, 13430 (2019)
28. C. Jacob, W. Anderson, Bound-Lay. Meteorol. **162**, 21 (2017)
29. D. Richter, P. Sullivan, Phys. Fluids **26**, 103304 (2014)
30. S. Rana, W. Anderson, M. Day, Geophys. Res. Lett. **47**, 088050 (2020)
31. G. Li, J. Zhang, H.J. Herrmann, Y. Shao, N. Huang, Geophys. Res. Lett. **47**, 086574 (2019)
32. R. Mathis, I. Marusic, S. Chernyshenko, N. Hutchins, J. Fluid Mech. **715**, 163 (2013)
33. B. Sun, B. Ma, P. Wang, L. Jian, C. Gao, Smart. Mater. Struct. **29**, 3 (2020)
34. J. Zhang, Y. Shao, N. Huang, Atmos. Chem. Phys. **14**, 8869 (2014)
35. B. Sun, B. Ma, J. Luo, B. Li, C. Jiang, J. Deng, Sensor Actuat. A-Phys. **265**, 217 (2017)
36. B. Walter, C. Gromke, K. Leonard, A. Clifton, M. Lehning, J. Wind Eng. Ind. Aerodyn. **104–106**, 314 (2012)
37. N. Huang, X.J. Zheng, Y.H. Zhou, Adv. Eng. Softw. **37**, 32 (2006)
38. R.A. Bagnold, *The Physics of Blown Sand and Desert Dunes* (Methuen, New York, 1941)
39. R. Kawamura, *Study of sand movement by wind* (University of California Hydraulics Engineering Laboratory Report HEL 2-8, Berkeley, 1965)
40. O. Durán, V. Schwämmle, P.G. Lind, H.J. Herrmann, Nonlinear Proc. Geoph. **18**, 455 (2011b)
41. I. Marusic, W. Heuer, Phys. Rev. Lett. **99**(11), 114501 (2007)
42. J. Komminaho, M. Skote, Flow Turbul. Combust. **68**, 167 (2002)
43. J. Österlund, *Experimental Studies of Zero Pressure-Gradient Turbulent Boundary Layer* (KTH, Stockholm, 1999). ((**PhD thesis**)
44. P. Schlatter, R. Örlü, J. Fluid Mech. **659**, 116 (2010)
45. E. Newland, *Random Vibrations and Spectral Analysis*, 2nd edn. (Longman, London, 1984)
46. A. Baas, D. Sherman, J. Geophys. Res.: Earth Surface **110**, F03011 (2005)
47. S. Dupont, G. Bergametti, B. Marticorena, S. Simoens, J. Geophys. Res-Atmos. **118**, 7109 (2013)
48. J. Hunt, J. Morrison, Eur. J. Mech B-Fluid **19**(5), 673 (2000)
49. A. Hilgers, C. Beck, Phys. Rev. E **60**, 5385 (1999)
50. A. Hilgers, C. Beck, Physica D **156**, 1 (2001)
51. G. Lewis, H. Swinney, Phys. Rev. Stat. Phys. Plasmas Fluids Relat. Interdiscip. Topics **59**, 5457–67 (1999)
52. C. Beck, E. Cohen, Physica **322**, 267 (2002)
53. C. Beck, E. Cohen, H. Swinney, Phys. Rev. E **72**, 056133 (2005)